Resilience of radial carpet beams under propagation through indoor convective air turbulence

Saifollah Rasouli[1,2,*] and **Mohammad Bagheri**[1]

[1] Department of Physics, Institute for Advanced Studies in Basic Sciences (IASBS), Zanjan 45137-66731, Iran
[2] Optics Research Center, Institute for Advanced Studies in Basic Sciences (IASBS), Zanjan 45137-66731, Iran

E-mail: rasouli@iasbs.ac.ir

CrossMark

Abstract

In this work, we investigate and compare propagation of Laguerre–Gaussian (LG) and the recently introduced radial carpet (RC) beams through an indoor convective air turbulence under weak to strong turbulence conditions. By determining the radial displacement of the intensity maxima over the donut ring of the LG beam, and tracing the radial coordinates of the main intensity spots of the RC beam, when the beams are propagating through the turbulence, we estimate the variance of the local displacements for both of the beams in the radial direction. It is shown that, under the same turbulence conditions, the RC beam experiences less disturbance and is more resilient to turbulence, especially when it has a complicated structure. The measured values of the image displacement variance for the RC beam are almost one order of magnitude smaller than the same parameter for the LG beam. In addition, for the LG beam, the symmetry of the beam is broken and in many places the intensity ring is even cut off. Although there are slight changes in the RC beams transverse intensity distribution, the number of the main intensity spots rarely changes. This feature makes the RC beam a good candidate for the transmission of information. We also show that a set of RC beams having different values of the main intensity spots (generated with different radial gratings having different spoke numbers) can be used as an orthogonal bases for free-space optical communication.

Supplementary material for this article is available online

(Some figures may appear in colour only in the online journal)

1. Introduction

Propagation of laser beams through a turbulent atmosphere has been widely used for a variety of purposes, including free-space optical communication (FSOC), remote sensing of the atmosphere, and target tracking [1, 2]. The use of a laser beam to transmit information in the free-space has some advantages. This kind of communication link is cost-effective, has higher security, and can be used between non-fixed locations [3, 4]. In recent years, propagation of laser beams through a turbulent atmosphere has received more attention [5–13], and FSOC has found many applications in military networks, communications between spacecraft, interplanetary communications, and security programs [14, 15].

---

[*] Author to whom any correspondence should be addressed.

Fluctuations of the temperature and pressure in the atmosphere, and existence of wind, are the main sources of turbulence in the atmosphere. These factors cause random changes in the refractive index of the atmosphere and is called optical turbulence. The spatial and temporal fluctuations of the refractive index give rise to three major effects on the laser beam passing through the atmosphere; angle of arrival (AA), intensity fluctuations, and beam wandering [16, 17]. Another major effect of the turbulence on the beam is wavefront distortion. The random changes in the refractive index result in time-varying intensity and phase profiles over the wavefront. In particular, major random fluctuations of the amplitude and phase of the wavefront prevent the use of the laser beams as information transmitters for FSOC. Fortunately, the structured beams having complicated wave forms, show nondiffracting and self-healing properties [18, 19]. A beam is said to be self-healing, if it can preserve its wave form under propagation, after canceling a part of the beam by an obstacle or when it propagates through a disturbing medium such as a turbulent atmosphere. In a considerable number of research work, the propagation of nondiffracting beams such as Bessel beams [20, 21], Laguerre–Gaussian (LG) beams [22, 23], Bessel–Gaussian beams [24, 25], Airy beams [26, 27], C-point and V-point beams [28], asymmetric Schell-model beams [29], Hermite non-uniformly correlated beams [30] and hyperbolic sinusoidal Gaussian beams [31] through turbulent atmospheres has been investigated.

Based on the complexity of the intensity and phase structures of the radial carpet (RC) beams [18, 19], we were motivated to investigate the propagation of these beams through atmospheric turbulence. Specifically, the existence of a considerable number of similar high-intensity spots over the central part of such beams makes them a good candidate to be used as a set of orthogonal bases for FSOC.

In this work, we produce LG and RC beams by diffracting a plane wave off fork linear and amplitude/phase radial gratings, respectively, and allow them to pass through an indoor convective air turbulence, and determine the beams' image motions/distortions by estimating the displacements of their local intensity maxima. We consider the overall displacement of the image under time as the image motion, and the local and relative displacement of the image points as the image distortion. We also examine the persistence of the overall shape of the wavefront by counting the number of the main spots on the RC beams after passing through the turbulent medium.

2. Governing equations and experimental setup

Schematic diagram of the experimental setup used to investigate propagation of RC and LG beams in an indoor convective air turbulence is shown in figure 1. The second harmonic of a neodymium-doped yttrium aluminum garnet (Nd:YAG) diode-pumped laser beam with a wavelength $\lambda = 532$ nm passes through a spatial filter and is collimated with a lens having a focal length 20 cm. The collimated laser beam passes through an amplitude or phase radial grating to generate the desired RC beam.

An amplitude radial grating can be produced by printing following transmission function on a transparent sheet:

$$t_a(r,\theta) = \frac{1}{2}\{1 + \text{sgn}[\cos(m\theta)]\}, \tag{1}$$

where m, r, and θ, show the grating spokes number, radial coordinate (here there is no such dependency), and azimuthal angle, respectively, and sgn is the sign function.

By passing a coherent plane wave through an amplitude radial grating, the complex amplitude of the diffracted light beam after a propagation length of z can be written as [18]:

$$\psi(r,\theta;z) = \frac{e^{ikz}}{2}\left\{1 + R'\sum_{s=1}^{+\infty}\psi_s\left[J_{\frac{sm+1}{2}}(R^2)\right.\right.$$
$$\left.\left. + iJ_{\frac{sm-1}{2}}(R^2)\right]\cos(sm\theta)\right\}, \tag{2}$$

where k is the wave number and is given by $\frac{2\pi}{\lambda}$, λ is the wavelength, $R' = Re^{iR^2}$, $R = r\sqrt{\frac{\pi}{2\lambda z}}$, $\psi_s = \sqrt{2\pi}(-i)^{\frac{ms}{2}+1}\text{sinc}(\frac{s\pi}{2})$, J indicates the Bessel function, and $s = 1, 2, 3, \ldots$.

Equation (2) shows the complex amplitude of the light field at propagation distance z. For a constant value of R, the diffraction pattern remains unchanged, although the other two parameters, including propagation distance, z, and radial coordinate, r, change. As the diffracted complex amplitude is an explicit function of R, the form of the produced optical pattern remains invariable during propagation. Since the distribution of the light field in equation (2) is shape invariant under propagation it can be considered as a beam and know as the RC beam [19, 32].

The same structure of equation (1) can be imposed on an SLM to generate a phase radial grating. We used a conventional SLM extracted from a video projector (LCD projector KM3, Model No. X50) to prepare the desired pure phase gratings. In this case, a binary phase profile with the following form is created on the SLM:

$$t_p(\theta) = e^{i\gamma\,\text{sgn}[\cos(m\theta)]}. \tag{3}$$

Here γ shows the amplitude of the phase variation.

By passing a coherent plane wave through this phase structure, the complex amplitude of the diffracted light beam after a propagation length of z can be written as [19]

$$\psi(r,\theta;z) = e^{ikz}\left\{\cos(\gamma) + R'\sum_{\substack{s=1\\odd}}^{+\infty}\phi_s\left[J_{\frac{sm+1}{2}}(R^2)\right.\right.$$
$$\left.\left. + iJ_{\frac{sm-1}{2}}(R^2)\right]\cos(sm\theta)\right\}, \tag{4}$$

where $\phi_s = \frac{2}{s}\sqrt{\frac{2}{\pi}}\sin(\gamma)(-i)^{(\frac{m}{2}-1)s+1}$. Here again the distribution of the light field in equation (4) is shape invariant under
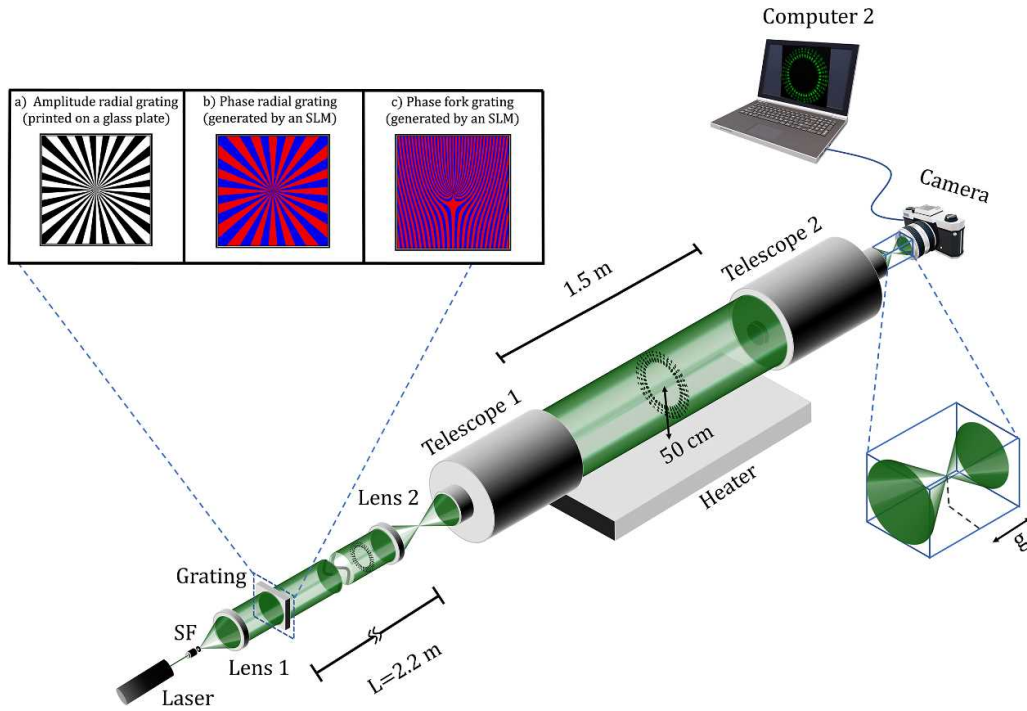
Figure 1. Schematic diagram of the experimental setup. Indoor convective air turbulence is created with a flat plate heater. In the left inset, three different gratings are shown: (a) illustrates an amplitude radial grating with a binary profile that can be printed on a sheet glass, (b) shows a phase radial grating with a binary profile that can be generated by an SLM, and (c) presents a binary phase fork grating that also can be generated by an SLM. These gratings were used one by one to generate different RC and LG beams in the setup. The second inset shows the location of the CCD.

propagation, and know as the RC beam. Since we derived propagation of these beams with the aid of Fresnel's integral [18, 19] and wave equation [32], these beams satisfy the paraxial wave equation.

We also produce an LG beam with a zero value of the radial index $p = 0$ in the diffraction of a plane wave from a phase fork linear grating by imposing an amplitude fork linear grating having the following transmission function on the SLM:

$$t_f(r,\theta) = \frac{1}{2}\left\{1 + \text{sgn}\left[\cos\left(\frac{2\pi x}{d} + l\theta\right)\right]\right\}, \quad (5)$$

where d is the grating period, l is an integer number denoting dislocation of the grating lines that we call it topological defect number of the grating. The value of l in this paper is 20.

In this case, a binary phase fork linear grating with the following form is created on the SLM:

$$t_{fp}(r,\theta) = e^{i\gamma sgn[\cos(\frac{2\pi x}{d} + l\theta)]}. \quad (6)$$

In general, the complex amplitude of an LG beam after a propagation length of z can be written as

$$\psi(r,\theta;z) = \frac{C_{LG(p,l)}\omega_0}{\omega(z)}\left(\frac{r\sqrt{2}}{\omega(z)}\right)^{|l|}L_p^{|l|}\left(\frac{2r^2}{\omega^2(z)}\right)$$

$$\times e^{\frac{-r^2}{\omega^2(z)} - \frac{ikr^2z}{2(z^2+z_R^2)}}e^{i(2p+|l|+1)\zeta(z)}e^{il\theta}, \quad (7)$$

where $C_{LG(p,l)} = \sqrt{2p!/(\pi(p+|l|)!)}$ is a normalization constant, L_p^l is the generalized Laguerre–Gauss polynomial of p (radial mode) and l (angular mode), $\zeta(z) = \arctan(z/z_R)$ is the Gouy phase, $\omega(z) = \omega_0\sqrt{1+(z/z_R)}$ is the beam radius, ω_0 is the beam waist, and $z_R = \pi\omega_0^2/\lambda$ is the Rayleigh range. It is important to note that the azimuthal phase profile, expressed as $e^{il\theta}$, is what allows these beams to exhibit OAM. In this work, we generate an LG beam with the OAM modes $l = 20$ and $p = 0$ by imposing transmission function of equation (6) on an SLM.

Figure 2 shows calculated intensity and phase distributions of the diffracted field from binary amplitude, binary phase, and fork gratings using equations (2), (4), and (7) and they correspond to the intensity and phase profiles of the RC and LG beams.

As it is seen from figure 2, the phase and intensity profiles of the RC beams have a considerable number of discontinuities or jumps in both radial and azimuthal directions. This feature says that these beams have very complex structures. It seems that such complexity helps the RC beams to retain their intensity profiles better than the LG beams when propagating in a turbulent atmosphere.

As shown in figure 1, two Cassegrain–Schmidt telescopes were used in experimental setup. It is worth mentioning that with the same arrangement, a pair of two-telescopic system, different turbulence conditions have been investigated [33, 34]. In order to fix constant the diameter of the beam, as it propagates through the turbulent area, the output light from the first telescope is collimated. For this purpose, we used a
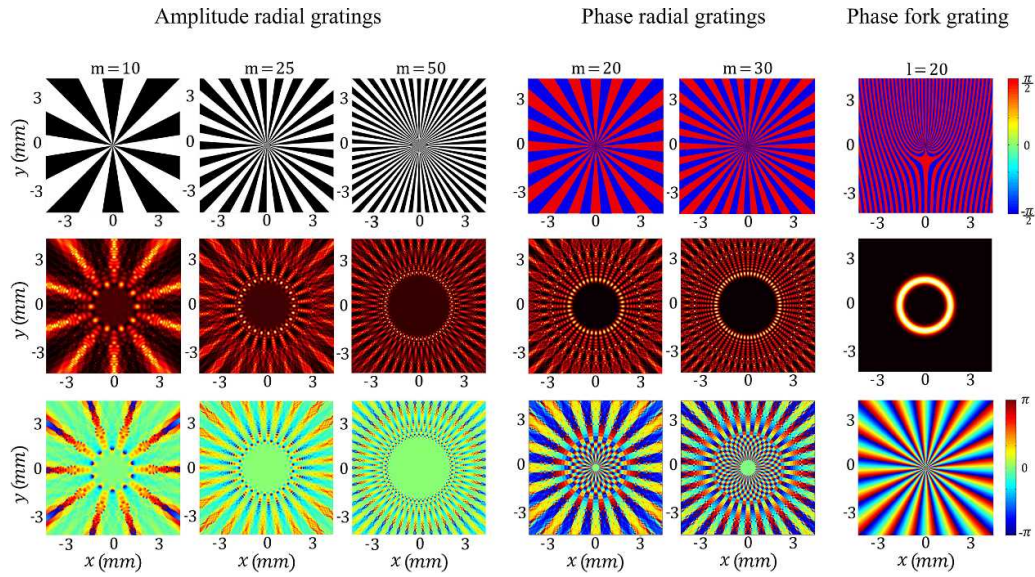
Figure 2. (First row) In the first to third columns the transmission profiles of three radial gratings with pure amplitude profiles are displayed. These patterns are generated using equation (1) and printed on transparent sheets for use in the experiments. In the fourth and fifth columns the transmission profiles of two radial gratings with pure phase profiles generated using equation (3) are shown. To generate the RC beams, these patterns are imposed on the SLM. In the last column, using equation (6) the transmission profile of a phase fork grating is depicted. This phase pattern can be imposed on the SLM for the generation of the LG beam. The spoke number m for the radial gratings and the dislocation of the fork grating lines l are written over the transmission profiles. For the radial and fork phase gratings, the value of the amplitude of the phase variation, γ, was $\pi/2$. (Second and third rows) The calculated intensity and phase distributions of the diffracted field when a plane wave passes through each of the transmission profiles are illustrated in the first row and propagate a distance $z = 100$ cm. The patterns of the first to the third columns were generated using equation (2), the patterns of the fourth and the fifth columns were generated using equation (4), and the pattern of the sixth column was plotted using equation (7).

lens with a focal length of 75 mm, before the first telescope. An indoor convective air turbulence is created by a heater with dimensions 50 cm × 100 cm that was equipped with a thermometer. The temperature of the heater can be adjusted by its driver. The heater is equipped with an internal thermometer that measures the temperature inside, and it is also equipped with a control system. There is also a temperature display on the control system. Using the control system, the desired temperature is transmitted to the device, which starts to heat up. When the internal temperature of the device reaches the desired temperature, the system turns itself off, but the internal temperature of the heater will still increase and its instantaneous temperature is shown on the device display. We wait for the heater temperature to slowly decrease and reach the desired target. In practice we have observed that, the heater temperature remains almost constant for more than 2 min at each temperate recursion time, which is a good interval to capture data. As the light propagates through the turbulent area, its amplitude and phase experience random fluctuations. As a result, over entrance aperture (pupil) of the second telescope, the AA of the beam at different points will depend on the strength of the turbulence. In addition, as the beam has an almost dynamic form at the entrance aperture of Telescope 2, its points will wander on that plane. These two effects cause image motion/distortion on the image plan where a CCD camera is placed.

The light passing through the turbulent medium is focused by the second telescope, and the beam intensity profiles are recorded in video format by a Nikon D7200

camera at 60 frames s^{-1}. The camera has a sensitive area 1.56 cm × 2.35 cm with a number of active pixels 720 × 1280 at the movie recording condition. Each pixel has a length 21 μm. The camera is installed at a distance 19 cm after the focal plane of the second telescope in which the full cross section of the beam covered by the sensitive area of the camera. At this distance, a number of 650 × 650 active pixels of the camera covers the full area of the beam impinging on it. The second telescope has an entrance pupil 28 cm and focal length 2.8 m. We record the beam intensity profile directly over the sensitive area by removing imaging lens of the camera. In each data set, we recorded a number of 3600 successive frames and analyzed them by MATLAB software.

It is worth noting that the physics of imaging a structured and non-diffracting beam through a turbulent medium seems a bit different from the imaging of a single star with a telescope again through turbulence. In the imaging of a star by a telescope with an aperture diameter smaller than the Fried parameter, the image motion is generated only by the AA fluctuation of the beam on the entrance aperture. When the Fried parameter is smaller than the aperture diameter, the star image blurs and also moves because the AA fluctuation that occurs at the entrance aperture. While, as can be seen in figure 3, the wandering of the different parts of a structured beam such as an RC beam at the entrance aperture of a telescope, can also cause image motion/distortion even when the AA of the beam remains unchanged. The latter effect cannot be observed in the imaging of a star when its plane wave enters a telescope because it has no structured intensity distribution on
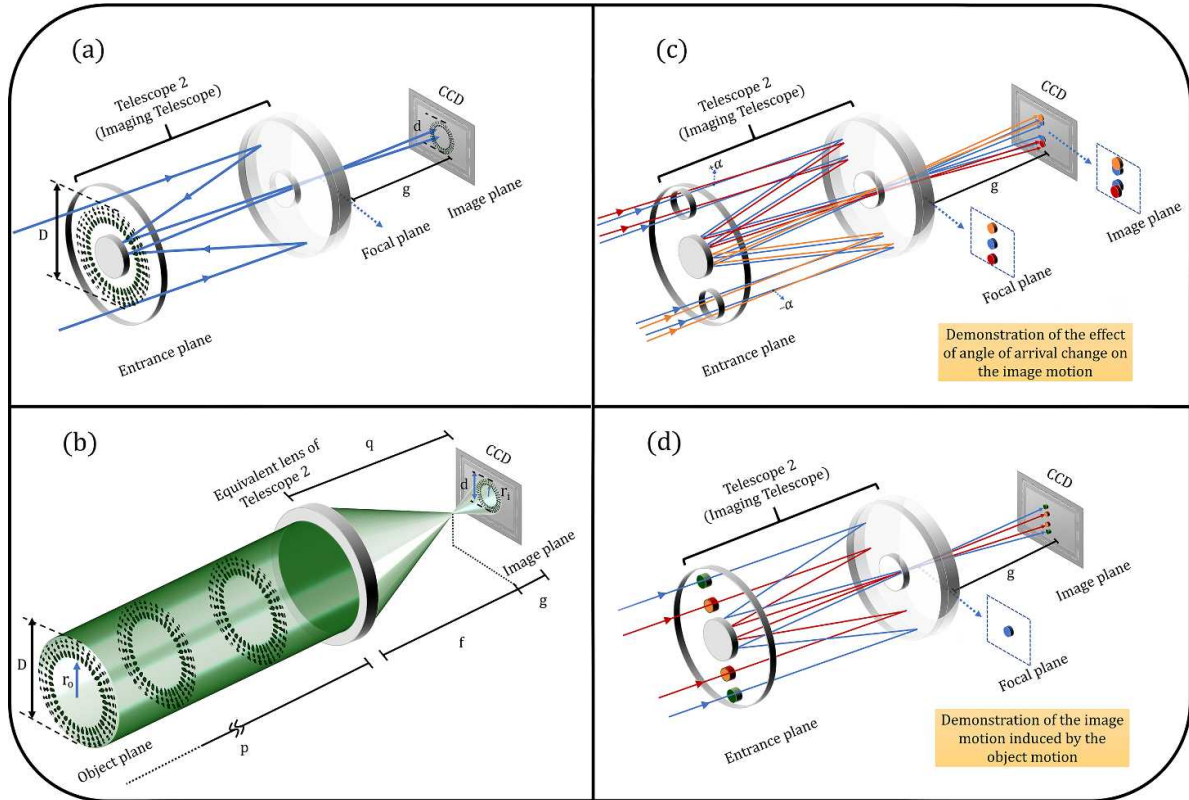
Figure 3. (a) Illustration of the imaging of a structured beam by a Cassegrain–Schmidt telescope, where g shows the distance between the focal and image planes. (b) Imaging of a structured beam by an equivalent lens of the Cassegrain–Schmidt telescope, where p and q show the distances of the object and image planes from the equivalent lens, respectively. Here, the object plane is far from the equivalent lens, and imaging occurs through turbulence. We denote the radial coordinate of a given point on the beam over the eject plane by r_o and that of the corresponding point at the image plane by r_i. (c) Illustration of the effects of different AA fluctuations on the image motion/distortion. It is seen that two locally different AA fluctuations (with equal values and different signs) cause two displacements of the image points in different directions both on the focal plane and on the image plane. (d) Illustration of the effect of the wandering of the structured beam on the image motion/distortion. Here we see that the displacement of two given points on the beam toward lower radial distances, causes their images also to displace to the lower radial distances on the image plane.

the transverse plane. Therefore, in the current work, the beam motion and its dynamics at the image plane have two distinct origins; the AA fluctuations of the beam on the entrance pupil of Telescope 2 and the beam wandering on the same plane (see figures 3(a)–(d)). For a given point on the structured beams entering Telescope 2, both of these effects cause an image motion/distortion on the CCD plane. Both these effects are due to the imaging of the transverse intensity profile of the structured beam through turbulence by the second telescope (Telescope 2). In fact, Telescope 2 images the beam intensity profile from the object plane (located far from Telescope 2) through the turbulent medium on the image plane located on the CCD's sensitive plane (figure 3(b)). Based on these facts, we report the measurement of the local displacements of the image points at different locations for the imaged RC and LG beams.

We determine the diameter of the imaging part of the beams on the sensitive area of the camera, d, by counting the number of pixels covering the diameter of the beam image, n, and multiply it by the pixel length d_p, $d = nd_p$. In all of the experiments, the values of the beam image diameter before Telescope 1 and after Telescope 2 were measured to be 8

and 13.8 mm, respectively. The diameter of the beams in the turbulent medium (between the telescopes) was equal to the aperture diameter of Telescope 1, $D = 20.32$ cm (see figure 3). The magnification factor for the combination of Telescope 1 (model MEADE lx200) and Lens 2 was 25 and the magnification of Telescope 2 (model CELESTRON Nexstar) for the images of the beams' intensity profiles at the image plane was 0.06.

2.1. Measurements and results

Figure 4 shows the intensity profiles of experimentally produced LG and RC beams. First column shows the intensity profiles before the first telescope and the other columns show the corresponding intensity profiles after passing through both turbulence medium and second telescope at different temperatures of the heater. LG beam of the first row, was produced in the propagation of a plane wave from a phase fork linear grating having topological defect number $l = 20$. If an LG beam having a lower value of l is used, then the central part of the beam is blocked by the secondary mirror of Telescope 1, and accordingly additional diffraction rings are generated
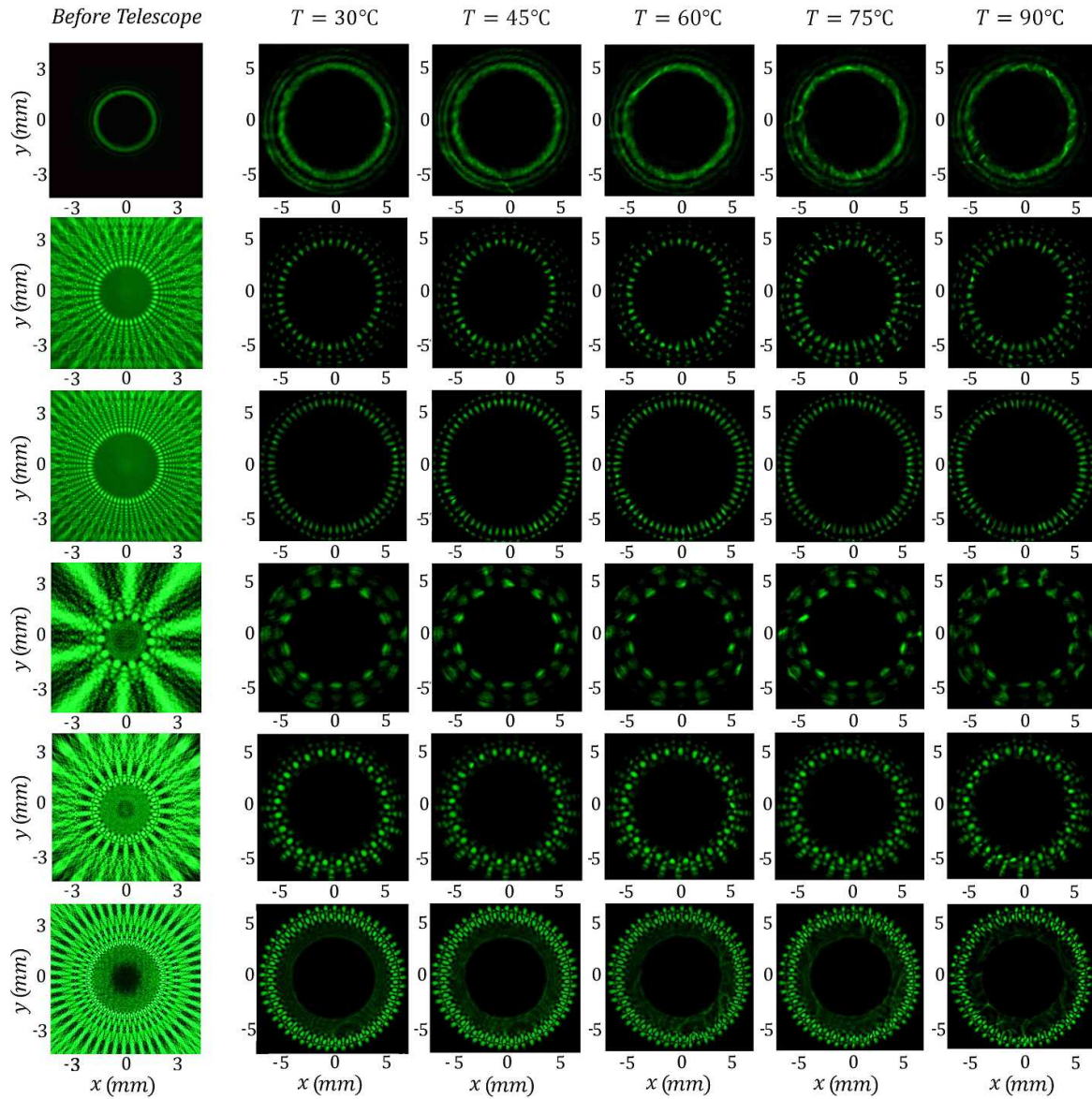
Figure 4. Intensity profiles of experimentally produced LG (first row) and RC (other rows) beams. The first column shows the beam's intensity profiles before the first telescope at a distance $z = 100$ cm from the generating amplitude or phase gratings, and the other columns show the corresponding intensity profiles at the image plane after the beams' passage through the turbulence medium at different temperatures of 30, 45, 60, 75, and 90 °C. For all the profiles of the second to last columns, the camera was installed at a fixed place. The LG beam was produced in the propagation of a plane wave from a phase fork linear grating (generated by the SLM) having the topological defect number $l = 20$. The RC beams of the second and third rows were produced through the propagation of a plane wave from radial phase gratings (generated by the SLM) having spokes number $m = 20$ and $m = 30$, respectively. The RC beams of the forth to sixth rows produced in the propagation of a plane wave from amplitude radial gratings (printed on the transparent sheets) having spokes numbers $m = 10$, $m = 25$, and $m = 50$, respectively (see also supplementary data 1–6).

after the mirror. To avoid this problem we used an LG beam with $l = 20$.

RC beams of second and third rows were produced in the propagation of a plane wave from radial phase gratings having spokes number $m = 20$ and $m = 30$, respectively. RC beams of the forth to sixth rows were produced in the propagation of a plane wave from amplitude radial gratings having spokes number $m = 10$, $m = 25$, and $m = 50$, respectively. The temperature of the heater were 30, 45, 60, 75, and 90 °C for the beams illustrated in the second to sixth columns, respectively.

For the used setup, these temperatures of the heater cover weak to strong turbulence. The background supplementary data 1–6 (available online at stacks.iop.org/JOpt/24/075602/mmedia) show time-varying behavior of the beams' intensity profiles, and supplementary data 7 illustrates the detail process of measurements. It can be seen that, under the similar conditions, the RC beam encounters less disturbances and it is more resilient to turbulence, especially when it has a complicated structure (i.e. it was generated with a radial grating having larger number of spokes, m). We also see that, at higher temperatures, the

Table 1. The measured powers for the generated beams.

Beam type	Before telescope 1	After telescope 2	Power of one of the main spots after telescope 2
RC beam[a] ($m = 10$)	16.4 μW	1.4 μW	0.06 μW
RC beam[a] ($m = 25$)	17.8 μW	7.5 μW	0.12 μW
RC beam[a] ($m = 50$)	18.2 μW	6.6 μW	0.14 μW
RC beam[b] ($m = 20$)	1.63 μW	0.65 μW	0.01 μW
RC beam[b] ($m = 30$)	1.75 μW	0.7 μW	0.01 μW
LG beam[c] ($l = 20$)	0.12 μW	0.1 μW	—

[a] Generated by an amplitude radial grating.
[b] Generated by a phase radial grating.
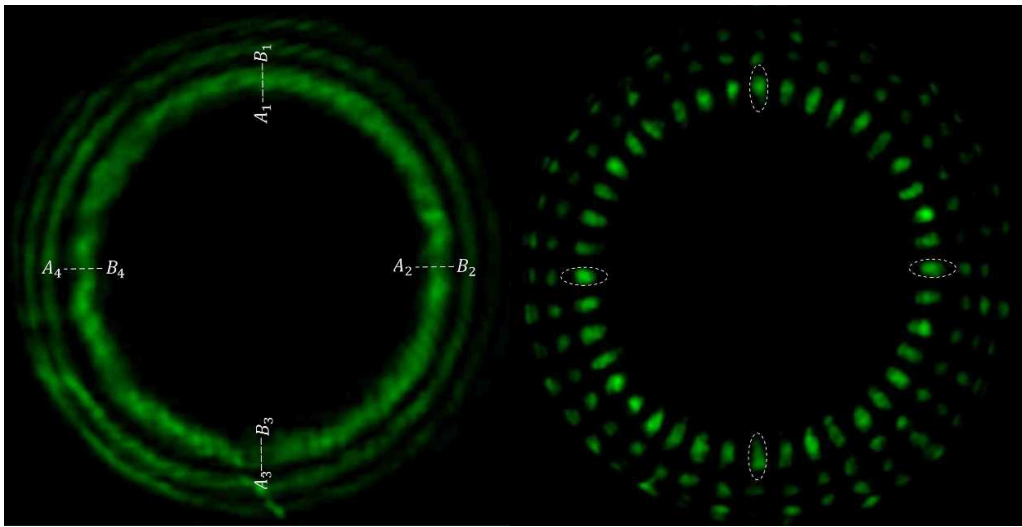[c] Generated by a phase fork grating.

Figure 5. Illustration of location of four points on the beams' cross sections used for the measurement of the displacements (the LG beam was generated by a phase fork grating with $l = 20$, and the RC beam was generated by a phase radial grating with $m = 20$ under plane wave illumination (both of the gratings are generated by the SLM)). The temperature of the heater was 45 °C.

symmetry of LG beam is broken and in many places its intensity ring even cuts off (see again supplementary data 2). For the RC beam, although there are slight changes over the intensity distribution, the number of main intensity spots remains unchanged (see again supplementary data 3–6).

The powers of the LG and RC beams generated with different grating structures, at the planes before Telescopes 1 and after Telescopes 2 are measured and presented in table 1. In addition, the power of one of the main spots of the RC beams after Telescope 2 was measured and presented in the last column of the same table. To have a better visibility for the beams' intensity profiles, we changed the exposure times in the video capture to improve the situation. The decrease in power is due to the blocking of high radius areas at the cross-section of the beam by the first telescope.

To reduce the volume of calculations, the displacements of four of the main spots of the RC beam locating at the top, bottom, left, and right sides of the central dark area, are measured.

Also, at the same locations over the donut ring of the LG beam, we determine radial coordinate of the maximum intensities and estimate the variance of displacements. These points correspond to the beams' paths having 40, 50, 50, and 60 cm altitudes from the heater surface. As the beams propagation direction in the turbulent medium is parallel with the heater surface and the beams have a diameter of 20 cm, different points of the beams along the vertical direction have different propagation paths and altitudes from the heater surface. The telescopes were installed face to face in the set-up in which their centers were located at an altitude of 50 cm from the heater surface. It is worth mentioning that the turbulence strength at the lower altitude is more than the upper one and the altitude used for the beams with the mentioned temperatures of the heater provide weak to strong turbulence. In figure 5 we represent intensity patterns presented in the first and second rows, third column, of figure 4, and illustrate four distinct locations we use the intensity distribution around them for the measurement of displacements.
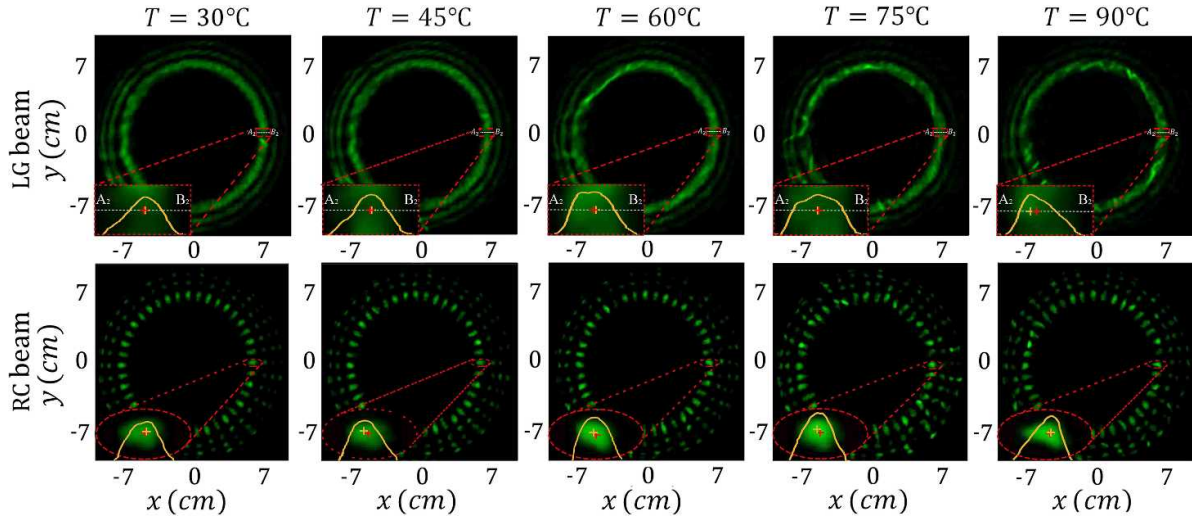
Figure 6. Insets show the one dimensional intensity profiles of the beams illustrated in the first and second rows of figure 2, in the radial direction over the donut ring of the LG beam and over one of the main spots of the RC beam. The yellow plus signs show the locations of the intensity maxima and the red plus signs show the locations of the intensity mass centers (for details see supplementary data 7).

In the measurements, we determine time-varying radius of donut ring (for the LG beam) and radial coordinates of maxima of the intensity spots (for the RC beams) illustrated on figure 5. It is worth noting that the precision of the image motion measurement can be smaller than the camera pixel size, if a sub-pixel algorithm is used (for details see [35]).

Using two approaches, one can determine radial displacement of a given main intensity spot of an RC beam and radial distance of a given point having maximum intensity on the donut ring form the center of an LG beam; determination of intensity mass center in the radial direction, or finding location of maximum intensity at the same direction. The first approach is more precise but it is a bit time-consuming respect to second one. To show that results of these approaches are very close, in figure 6 we determine the location of maximum intensities in the radial direction and the location of center of mass of intensity over the ring/spots for an LG beam with $l = 20$ and an RC beam with $m = 25$ after propagating through turbulent medium. The beams pass through turbulent medium having temperatures 45, 60, 75, and 90 °C.

In all of the recorded successive intensity profiles, the displacements of four determined main intensity spots in the radial direction (for the RC beams), and the displacements of the maximum intensities at the same locations in the radial direction (for the LG beam) have been measured. The calculated time series of the radial displacements, at different temperatures of the heater, for four sections of both LG and RC beams, are shown in figures 7 and 8. In figure 9 the same plots are only presented for the bottom side intensity maxima/spots of the beams. In each diagram, 3600 consecutive images were examined.

As it is seen in figure 7, at the room temperature, the measured values of $\sigma_{r_i}^2$ for both beams at four described sections are equal.

As it is shown in figure 8, by increasing the heater's temperature the values of $\sigma_{r_i}^2$ increase for both beams, but the increasing rate for the LG beam is larger. In addition, for the data of both beams recorded at the bottom sides of the beams, the displacements are lager, as these points are closer to the heat source. We also see that, at higher temperatures of the heater, the measured values of $\sigma_{r_i}^2$ for the RC beam, are almost one order of magnitude smaller the same parameter for the LG beam (for example, in figure 8 for $T = 90$ °C at the last row we have $\frac{(\sigma_{r_i}^2)_{LC}}{(\sigma_{r_i}^2)_{RC}} = \frac{41.65}{4.93} = 8.5$). This result can be interpreted as, under the same temperature conditions, the RC beam is more robust than the LG beam while passing through the same turbulent atmosphere.

For better comparison of behavior of induced displacements on LG beam generated by a phase fork grating with $l = 20$ (first column), RC beam generated by a phase radial grating with $m = 30$ (second column), and RC beam generated by an amplitude radial grating with $m = 50$ (third column), the measured radial displacements are plotted in figure 9. The temperature of the heater in these cases were 25 °C (room temperature), 30, 45, 60, 75, and 90 °C, and the displacements at the bottom side of the beams having a height 40 cm above the heater were examined. $\sigma_{r_i}^2$ for each data set is given at the top of graphs.

As it is shown in figure 9, the measured displacements for each beam increase with increasing the temperature, and under the same turbulence conditions, the RC beam experiences less disturbances. Figure 10 shows the calculated $\sigma_{r_i}^2$ with LG and RC beams at different temperatures of the heater. Plots show that the RC beams are more resilient to turbulence, especially when they have complicated structure (those with a large number of main intensity spots in the profile).
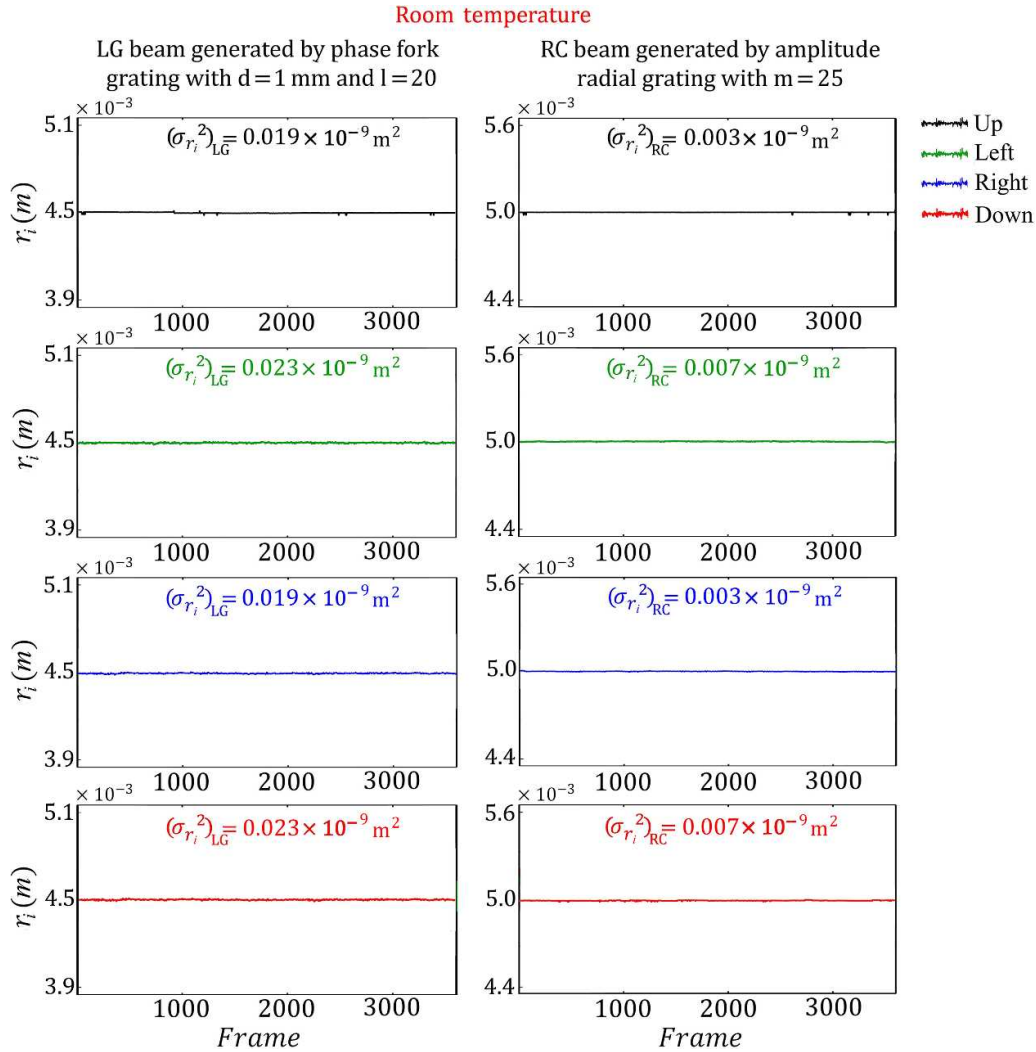
Figure 7. Calculated displacements for an LG beam generated by a phase fork grating with $l = 20$ (first column) and for an RC beam generated by an amplitude radial grating with $m = 25$ (second column) at room temperature. Top, left, right, and bottom stand for the locations of the four sections of the beams illustrated in figure 4 and correspond to the beams' paths having heights of 60, 50, 50, and 40 cm above the heater, respectively. $\sigma_{r_i}^2$ for each measurement is given at the top of the graph.

In figure 11, we show that a set of RC beams having different values of main intensity spots (generated with different radial gratings having different spokes numbers) can be used as a set of orthogonal bases for FSOC. To show this capability of the RC beams, we counted the number of main intensity spots at the end of turbulent medium at different temperature of heater. Figure 11 shows that the number of main intensity spots rarely changes. This feature make the RC beams a good candidate for the transmission of information.

The RC beams are nondiffracting, accelerating, and self-healing. The intensity patterns of the RC beams at the transverse plane are known as optical carpets. An RC beam and its corresponding optical carpet are generated immediately after the radial grating when a plane wave passes through it. The

optical carpets of the RC beams are shape invariant under propagation [18, 19]. The transverse size of an optical carpet at the start of the propagation expands rapidly, but the rate of expansion decreases during propagation. We know that the angular distribution of the far-field diffraction pattern for the convectional apertures remains invariant and the rate of the increment of the pattern size is constant with respect to z. Therefore, the above-mentioned fact is in contradiction with the conventional rules of diffraction optics. The singularity of the radial grating causes this violation of the conventional rules of diffraction optics. As the diffraction of the RC beams is less than the diffraction of conventional beams such as the Gaussian beams, we have used the non-diffractive term for them [18, 19, 32]. In this work we examined the propagation of the RC beams through turbulence, considered whether
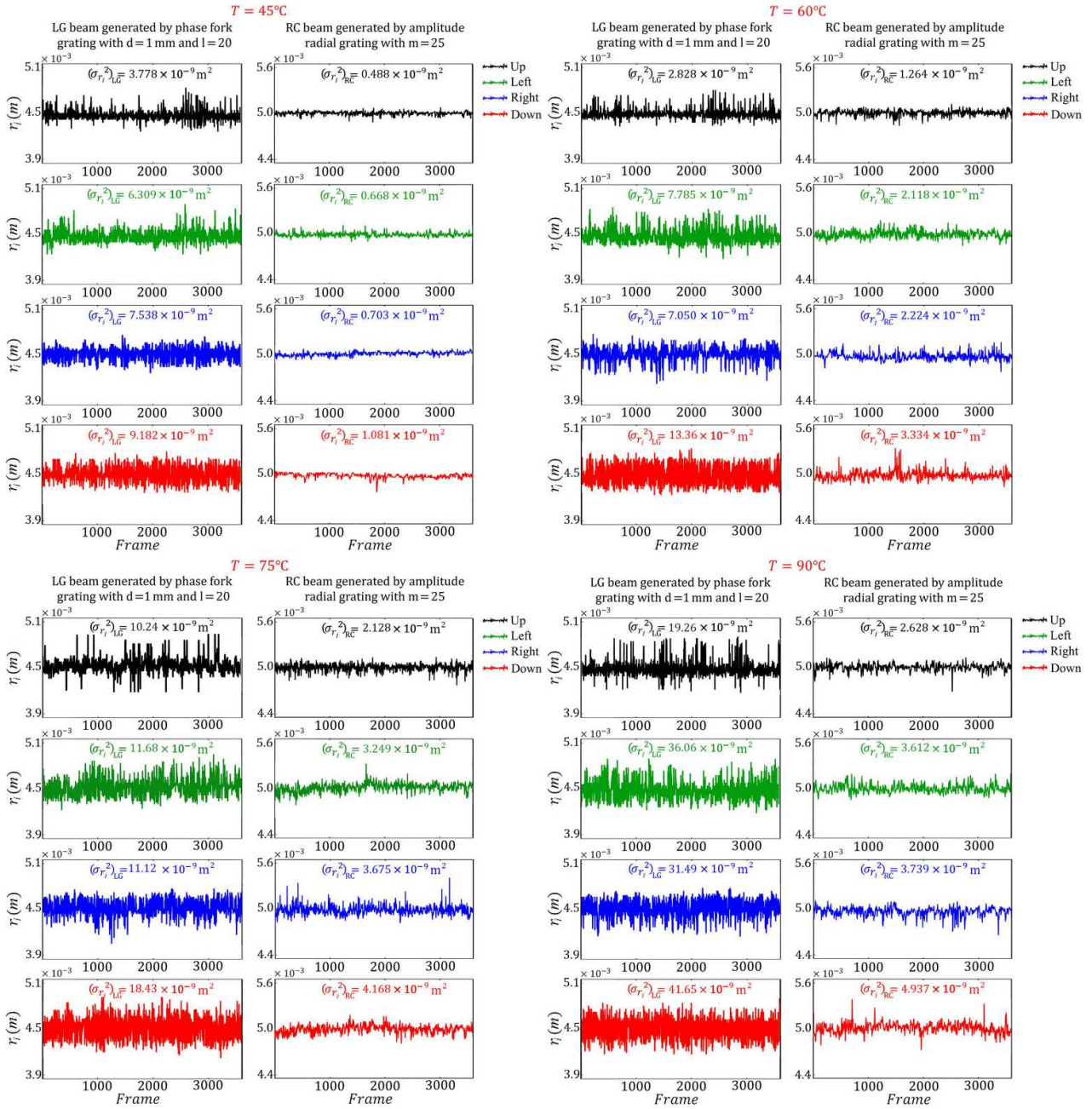
Figure 8. Calculated displacements for the same LG and RC beams of figure 7. The temperature of the heater in these cases were 45, 60, 75, and 90 °C. Here also, top, left, right, and bottom stand for the locations of the four sections of the beams illustrated in figure 5 and correspond to the beams' paths having heights of 60, 50, 50, and 40 cm above the heater, respectively. $\sigma_{r_i}^2$ for each measurement is given at the top of the graph.

the turbulence changes the shape of the RC beams under propagation, and according to figure 11, we see that in most of the cases studied the RC beams have retained their intensity distribution forms.

Finally, we show that propagation through turbulence disturbs the circular symmetry of the LG and RC beams. For the RC beams, by determining the intensity mass center of all of the main spots, and connecting them, we plot the trace of spots'

centers. As it is seen, although there are slight changes in the transverse profiles, the plotted traces are very close to circles. It is worth noting that the number of main intensity spots for an RC beam is twice the number of radial spokes of the radial grating when it is generated in the diffraction of a plane wave from a phase grating. But for the RC beams generated with amplitude radial gratings, these numbers are equal. For the LG beam, by determining the location of the maximum intensities
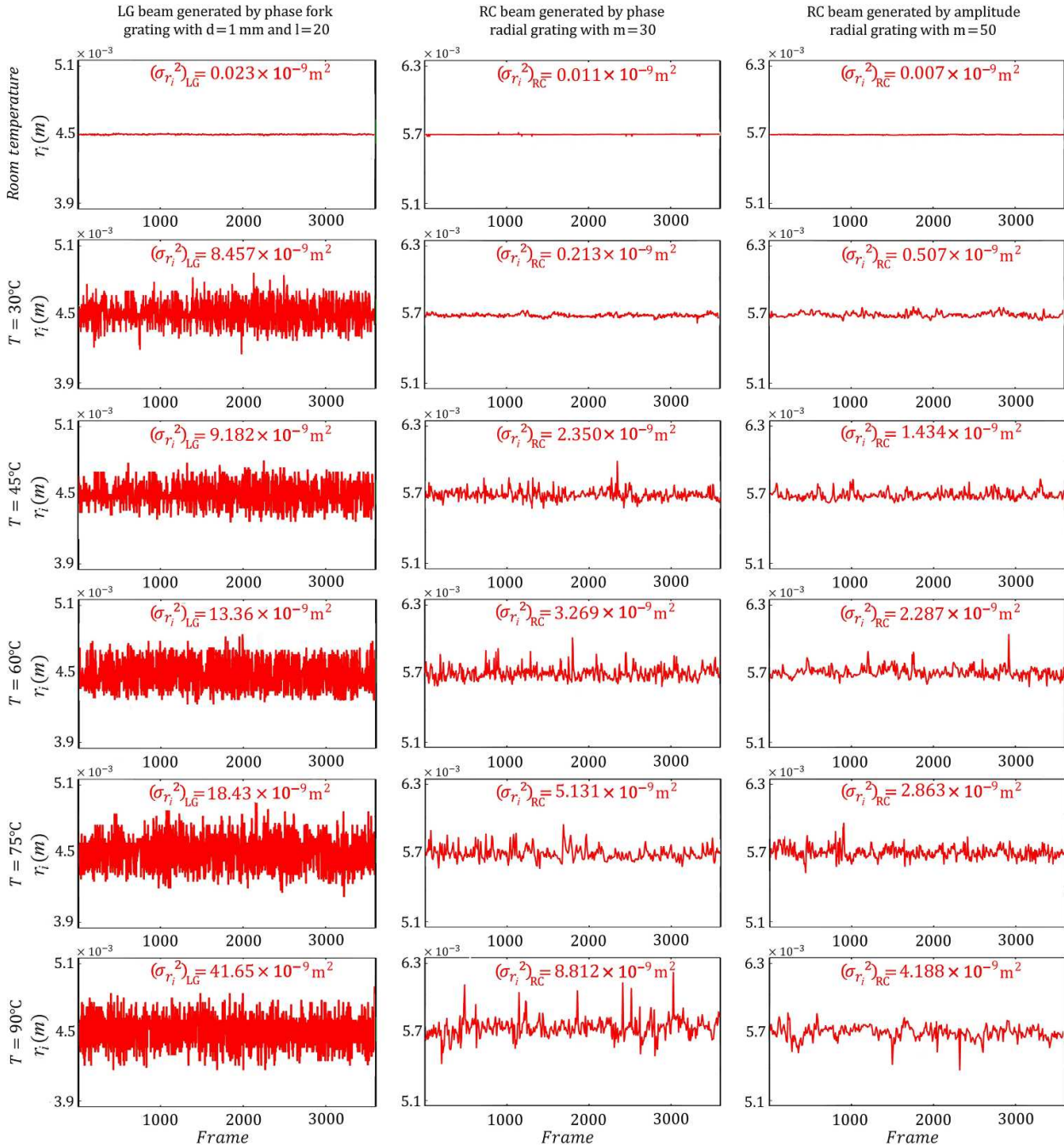
Figure 9. The displacements measured with LG beam generated by a phase fork grating with $l = 20$ (first column), RC beam generated by a phase radial grating with $m = 30$ (second column), and RC beam generated by an amplitude radial grating with $m = 50$ (third column) at different heater temperatures at the end of the turbulent medium. All measurements are for the light beams having a path height of 40 cm from the heater.

at each azimuthal angle and connecting them, we obtain the trace of maximum intensities over the donut ring. It is shown that the symmetry of LG beam was broken and in many places its trace experiences jumps and cuts. In figure 12, We use $\sigma_{r_i}^2$

for the frame, which shows the beam has deviated from its circular shape due to turbulence. Investigating the form variation of the beams from the ideal circular shape in time is under study.
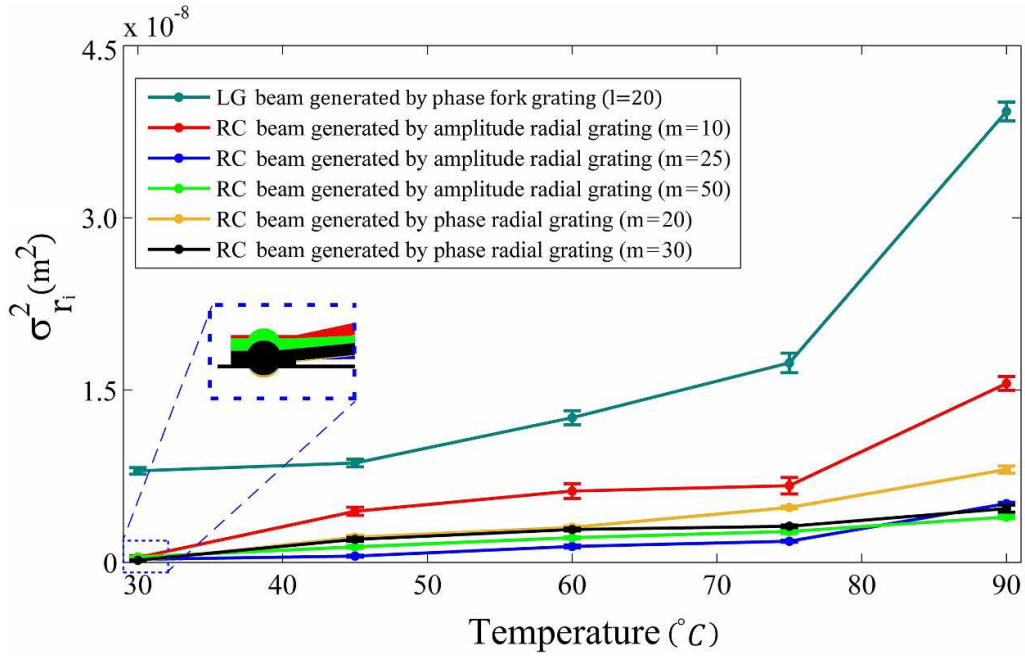
Figure 10. Calculated $\sigma_{r_i}^2$ for the LG and RC beams at different temperatures of the heater.
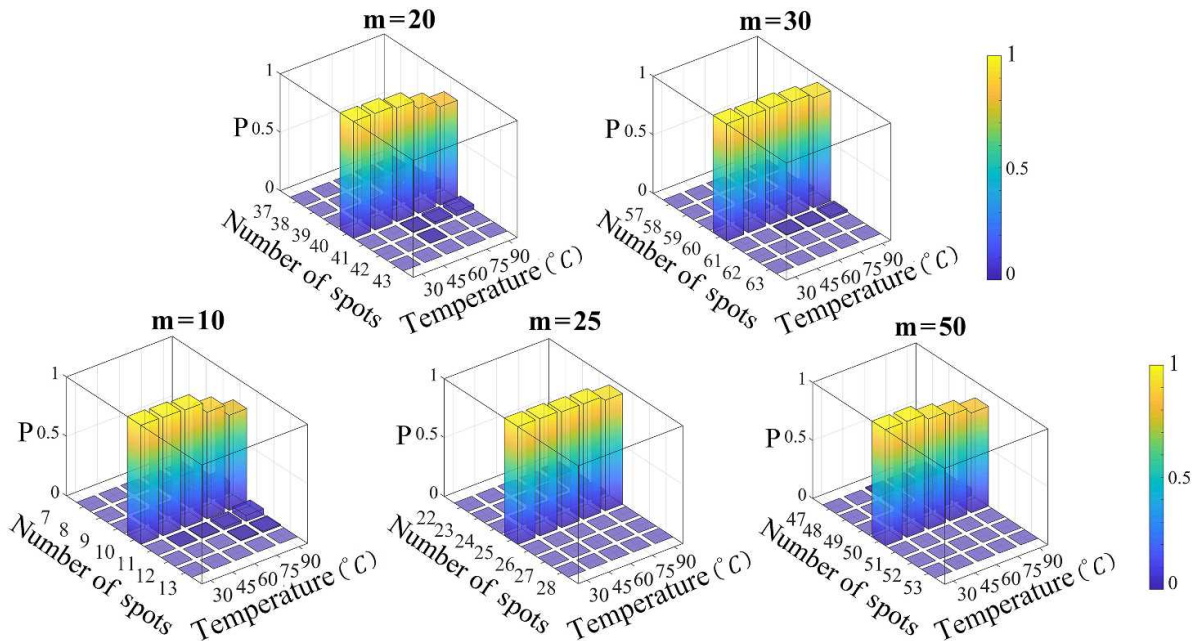

Figure 11. Relation of the number of the main intensity spots of the generated RC beams at the entrance plane and at the received plane at the end of turbulence medium for different values of the heater temperature. The first (second) row shows the results of the RC beams generated with phase (amplitude) radial gratings.
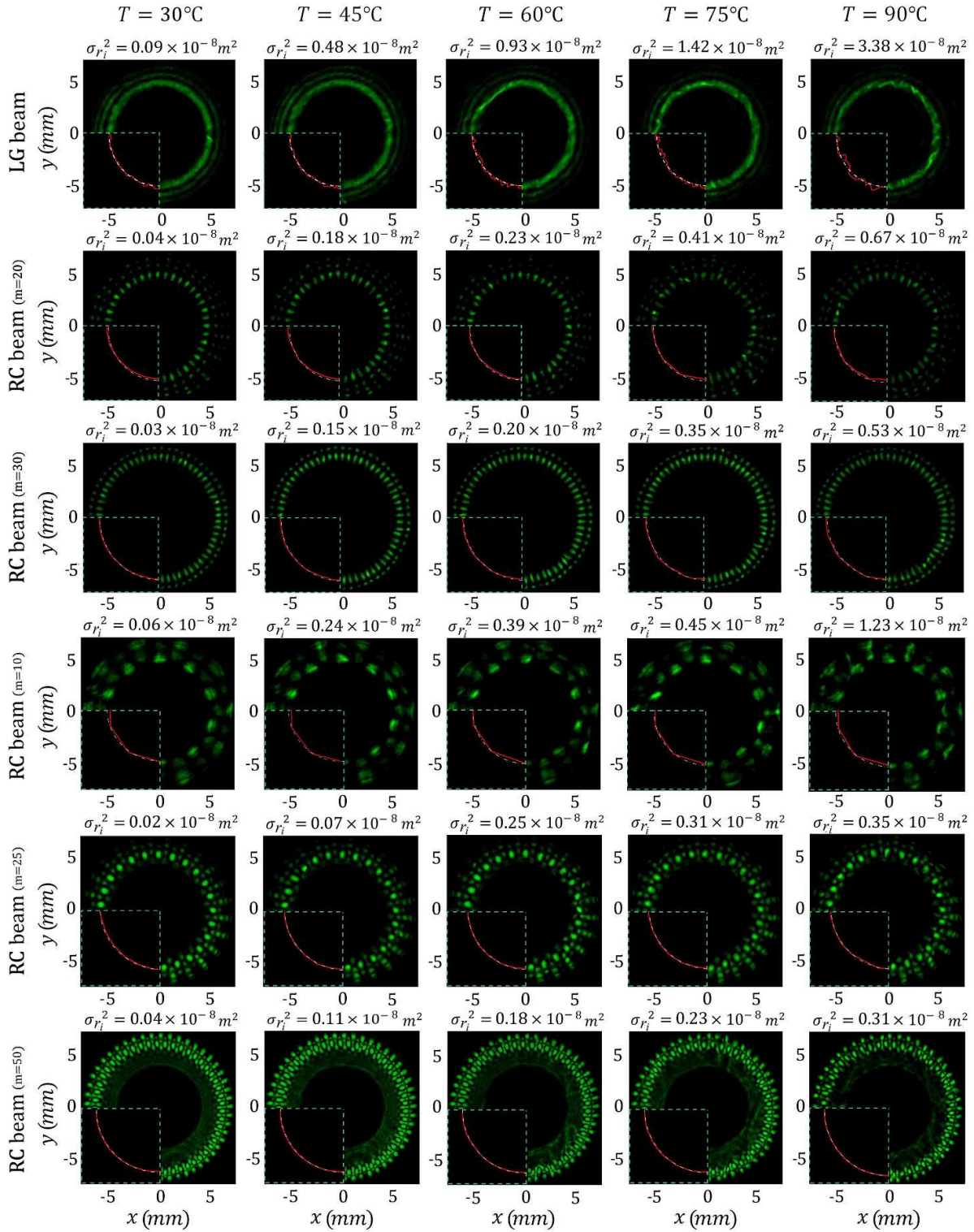
Figure 12. Investigation of the circular symmetry of the LG and RC beams. The red lines form with connecting the intensity mass center of all of the main spots for the RC beams and the maximum intensities at each azimuthal angle for the LG beam. In each plot, the circle closest to the red line trace is marked with a white circle. The beams of the second and third (fourth to six) rows were generated with phase (amplitude) radial gratings.

3. Conclusion

Propagation of LG and RC beams through an indoor convective air turbulence was studied. The radial displacements were calculated by chasing the locations of the beams' maximum intensities at different temperatures of the heater generating the turbulence. The measured values of $\sigma_{r_i}^2$ for the RC beams were found to be almost one order of magnitude smaller than

the same parameter calculated for the LG beam. This indicates that the RC beams are more resistant to turbulence. It is also shown that the number of main intensity spots of the RC beams under turbulence condition rarely changes. These features of the RC beams make them a good candidate for FSOC through turbulent atmospheres. We believe that this work will contribute significantly to the field of laser beam propagation through turbulence.

It is worth noting that, in the presented study the external area of the RC beams was canceled with the entrance aperture of the first telescope, this cancellation decreases the resilience property of the beams. It seems that by propagating the perfect RC beams, for example through a real atmospheric turbulence, their resilience will be increased. This issue is under study.

Data availability statement

The data that support the findings of this study are available upon reasonable request from the authors.

Acknowledgment

ORCID iD

Saifollah Rasouli ⬤ https://orcid.org/0000-0003-2703-8925

References

[1] Andrews L C and Phillips R L 1998 *Laser Beam Propagation in the Turbulent Atmosphere* (Bellingham, WA: SPIE Press)
[2] Ricklin J C and Davidson F M 2002 *J. Opt. Soc. Am.* A **19** 1794–802
[3] Toyoshima M 2005 *J. Opt. Netw.* **4** 300–11
[4] Juarez J C, Dwivedi A, Hammons A R, Jones S D, Weerackody V and Nichols R A 2006 *IEEE Commun. Mag.* **44** 46–51
[5] Korotkova O 2008 *Opt. Commun.* **281** 2342–8
[6] Cai Y and He S 2006 *Appl. Phys. Lett.* **89** 041117
[7] Noriega-Manez R J and Gutiérrez-Vega J C 2007 *Opt. Express* **15** 16328–41
[8] Eyyubolu H T 2008 *Opt. Laser Technol.* **40** 156–66
[9] Dan Y and Zhang B 2008 *Opt. Express* **16** 15563–75
[10] Dan Y and Zhang B 2009 *Opt. Lett.* **34** 563–5
[11] Mahdieh M H 2008 *Opt. Commun.* **281** 3395–402
[12] Yuan Y, Cai Y, Qu J, Eyyuboğlu H T, Baykal Y and Korotkova O 2009 *Opt. Express* **17** 17344–56
[13] Zhu S and Cai Y 2011 *Appl. Phys.* B **103** 971–84
[14] Henniger H and Wilfert O 2010 An Introduction to Free-space Optical Communications *Radioengineering* **19** 203–12
[15] Chan V W 2006 *J. Lightwave Technol.* **24** 4750–62
[16] Silbaugh E E, Welsh B M and Roggemann M C 1996 *J. Opt. Soc. Am.* A **13** 2453–60
[17] Rasouli S 2010 *Opt. Lett.* **35** 1470–2
[18] Rasouli S, Khazaei A M and Hebri D 2018 *J. Opt. Soc. Am.* A **35** 55–64
[19] Rasouli S, Khazaei A M and Hebri D 2018 *Phys. Rev.* A **97** 033844
[20] Birch P, Ituen I, Young R and Chatwin C 2015 *J. Opt. Soc. Am.* A **32** 2066–73
[21] Mphuthi N and Forbes A 2019 Bessel beams through turbulence *Frontiers in Optics + Laser Science APS/DLS Washington 15–19 September 2019* JTu3A.33
[22] Trichili A, Salem A B, Dudley A, Zghal M and Forbes A 2016 *Opt. Lett.* **41** 3086–9
[23] Wang F, Cai Y, Eyyuboglu H T and Baykal Y K 2010 *Prog. Electromagn. Res.* **103** 33–56
[24] Zhu K, Li S, Tang Y, Yu Y and Tang H 2012 *J. Opt. Soc. Am.* A **29** 251–7
[25] Chen B, Chen Z and Pu J 2008 *Opt. Laser Technol.* **40** 820–7
[26] Nelson W, Palastro J, Davis C and Sprangle P 2014 *J. Opt. Soc. Am.* A **31** 603–9
[27] Gu Y and Gbur G 2010 *Opt. Lett.* **35** 3456–8
[28] Lochab P, Senthilkumaran P and Khare K 2019 *Appl. Opt.* **58** 6335–45
[29] Liu S, Yang Y, Li J and Tang M 2021 *Optik* **243** 167407
[30] Yu J, Wang F, Liu L, Cai Y and Gbur G 2018 *Opt. Express* **26** 16333–43
[31] Bayraktar M 2021 *Microw. Opt. Technol. Lett.* **63** 1595–600
[32] Hebri D and Rasouli S 2018 *Phys. Rev.* A **98** 043826
[33] Razi E M and Rasouli S 2019 *Appl. Phys.* B **125** 185
[34] Rasouli S and Rajabi Y 2016 *Opt. Laser Technol.* **77** 40–50
[35] Dashti M and Rasouli S 2012 *J. Opt.* **14** 095704